

# Chapter 15

## Nanomechanics of Ferroelectric Thin Films and Heterostructures

Yulan Li, Shengyang Hu, and Long-Qing Chen

### 15.1 Ferroelectrics

Ferroelectricity was first observed by Valasek in 1920 in Rochelle salt [1]. Ferroelectricity refers to materials that possess a spontaneous electric polarization along a unique crystallographic direction with the additional property that the polarization can be reversed by the application of an external sufficiently strong electric field. Ferroelectrics are a group of materials that possess the property of ferroelectricity. The prefix *ferro*, meaning iron, was borrowed from ferromagnetism, as they both exhibit hysteresis loops, although most ferroelectric materials do not contain iron. Typically, materials only demonstrate ferroelectricity below a certain phase transition temperature, called the Curie temperature,  $T_c$ , and are paraelectric above this temperature. Ferroelectrics are very useful for devices and are used in many different ways today such as ferroelectric capacitors, random-access memory (RAM), and radio-frequency identification (RFID) cards.

Barium titanate ( $\text{BaTiO}_3$ ) is the most widely used ferroelectric material and is a member of the perovskite family, which is based on the mineral  $\text{CaTiO}_3$ .  $\text{BaTiO}_3$  has its titanium ion occupying the octahedrally coordinated site and the Ba ion in the 12-fold coordinated site in a high temperature  $\text{Pm}3\text{m}$  cubic symmetry. The ferroelectric phase at room temperature is tetragonal with oxygen and titanium ions shifting to produce a spontaneous polarization. As the temperature

---

Y. Li (✉) • S. Hu

Pacific Northwest National Laboratory, 902 Battelle Boulevard, Richland, WA 99352, USA

e-mail: [yulan.li@pnnl.gov](mailto:yulan.li@pnnl.gov); [shenyang.hu@pnnl.gov](mailto:shenyang.hu@pnnl.gov)

L.-Q. Chen

Pennsylvania State University, N-321 Millennium Science Complex, University Park,

PA 16802, USA

e-mail: [lqc3@psu.edu](mailto:lqc3@psu.edu)

© Springer International Publishing Switzerland 2016

C.R. Weinberger, G.J. Tucker (eds.), *Multiscale Materials Modeling*

for Nanomechanics, Springer Series in Materials Science 245,

DOI 10.1007/978-3-319-33480-6\_15

is reduced, BaTiO<sub>3</sub> undergoes a series of ferroelectric–ferroelectric transitions from tetragonal (P4mm) to orthorhombic (Bmm2), around 5 °C, and a transition from orthorhombic to rhombohedral (R3m) at around –80 °C [2, 3]. Recent theoretical and experimental studies showed that the ferroelectric transition temperatures and polarization magnitudes of an epitaxial BaTiO<sub>3</sub> thin film can be dramatically altered by a substrate constraint [4–7]. For example, it was recently discovered that a 1.7 % biaxial compressive strain on a (001)-oriented epitaxial BaTiO<sub>3</sub> thin film could increase its ferroelectric transition temperature to over 600 °C [6]. The ferroelectric transition between orthorhombic and rhombohedral phases at lower temperatures can disappear under a sufficiently large biaxial tension strain [8].

When a ferroelectric transition occurs from its original cubic paraelectric state to a tetragonal ferroelectric state, the spontaneous polarization can be parallel to one of the ⟨100⟩ directions of the cubic crystallographic directions resulting in a total of six tetragonal domains. Correspondingly, there are 12 possible domains in the orthorhombic phase with the spontaneous polarizations parallel to one of the ⟨110⟩ directions, and eight possible domains in rhombohedral phase with the spontaneous polarization parallel to one of the ⟨111⟩ directions, respectively. A domain refers to a region in the crystal that possesses the same polarization orientations. A typical feature of ferroelectrics is the formation of domain structures when a paraelectric phase is cooled through the ferroelectric transition temperature. The formation of domain structures in ferroelectric materials occurs to accommodate the boundary conditions imposed on the system thus to reduce the depolarization energy and the elastic energy of the material system. The interface between two different domains is called domain wall, which is a thin layer with a thickness usually of only several nanometers. For a given temperature, the stable phases are determined by the minimization of the bulk free energy. The bulk free energy density in the absence of any constraint can be expanded as a polynomial of the components  $P_i$  ( $i = 1, 2, 3$ ) of the polarization vector  $\mathbf{P} = (P_1, P_2, P_3)$  known as the Landau–Devonshire description [9–11]:

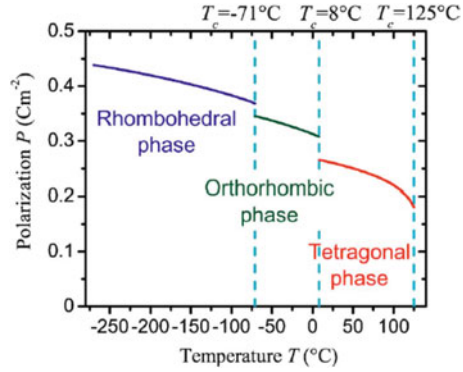
$$\begin{aligned} f_{\text{bulk}}(P_i) = & \alpha_1 (P_1^2 + P_2^2 + P_3^2) + \alpha_{11} (P_1^4 + P_2^4 + P_3^4) + \alpha_{12} (P_1^2 P_2^2 + P_2^2 P_3^2 + P_1^2 P_3^2) \\ & + \alpha_{111} (P_1^6 + P_2^6 + P_3^6) + \alpha_{112} [P_1^4 (P_2^2 + P_3^2) + P_2^4 (P_3^2 + P_1^2) + P_3^4 (P_1^2 + P_2^2)] + \alpha_{123} P_1^2 P_2^2 P_3^2 \\ & + \alpha_{1111} (P_1^8 + P_2^8 + P_3^8) + \alpha_{1112} [P_1^6 (P_2^2 + P_3^2) + P_2^6 (P_3^2 + P_1^2) + P_3^6 (P_1^2 + P_2^2)] \\ & + \alpha_{1122} (P_1^4 P_2^4 + P_2^4 P_3^4 + P_1^4 P_3^4) + \alpha_{1123} (P_1^4 P_2^2 P_3^2 + P_2^4 P_1^2 P_3^2 + P_3^4 P_1^2 P_2^2), \end{aligned} \quad (15.1)$$

where the coefficients  $\alpha_{ij}$ ,  $\alpha_{ijk}$ , and  $\alpha_{ijkl}$  are constants.  $\alpha_1$  is linearly dependent on temperature ( $T$ ) and obeys the Curie–Weiss law  $\alpha_1 = 1/(2\varepsilon_0\chi) = (T - T_0)/(2\varepsilon_0C)$ , where  $C$  is the Curie–Weiss constant,  $T_0$  is the Curie–Weiss temperature, and  $\varepsilon_0$  is the dielectric susceptibility of vacuum. For BaTiO<sub>3</sub>, these coefficients can be found in Ref. [12] and are listed in Table 15.1. The energy density of Eq. (15.1) with the given coefficients in Table 15.1 yields the transition temperatures  $T_{c(\text{Cubic} \leftrightarrow \text{Tetragonal})} = 125$  °C,  $T_{c(\text{Tetragonal} \leftrightarrow \text{Orthorhombic})} = 8$  °C, and  $T_{c(\text{Orthorhombic} \leftrightarrow \text{Rhombohedral})} = -71$  °C for stress-free BaTiO<sub>3</sub> single crystals. The polarizations as a function of temperature obtained from minimizing Eq. (15.1) are displayed in Fig. 15.1.

**Table 15.1** Coefficients of Landau–Devonshire description of Eq. (15.1) for BaTiO<sub>3</sub> where  $T$  is temperature in °C

Coefficients	Values	Units
$\alpha_1$	$4.124 \times 10^5 (T - 115)$	$\text{C}^{-2}\text{m}^2\text{N}$
$\alpha_{11}$	$-2.097 \times 10^8$	$\text{C}^{-4}\text{m}^6\text{N}$
$\alpha_{12}$	$7.974 \times 10^8$	$\text{C}^{-4}\text{m}^6\text{N}$
$\alpha_{111}$	$1.294 \times 10^9$	$\text{C}^{-6}\text{m}^{10}\text{N}$
$\alpha_{112}$	$-1.950 \times 10^9$	$\text{C}^{-6}\text{m}^{10}\text{N}$
$\alpha_{123}$	$-2.500 \times 10^9$	$\text{C}^{-6}\text{m}^{10}\text{N}$
$\alpha_{1111}$	$3.863 \times 10^{10}$	$\text{C}^{-8}\text{m}^{14}\text{N}$
$\alpha_{1112}$	$2.529 \times 10^{10}$	$\text{C}^{-8}\text{m}^{14}\text{N}$
$\alpha_{1122}$	$1.637 \times 10^{10}$	$\text{C}^{-8}\text{m}^{14}\text{N}$
$\alpha_{1123}$	$1.367 \times 10^{10}$	$\text{C}^{-8}\text{m}^{14}\text{N}$

**Fig. 15.1** Polarizations versus temperature in BaTiO<sub>3</sub> single crystal under stress-free condition, where  $P = |\mathbf{P}|$ ,  $\mathbf{P} = (0, 0, P_T)$  in tetragonal phase,  $\mathbf{P} = (P_O, 0, P_O)$  in orthorhombic phase,  $\mathbf{P} = (P_R, P_R, P_R)$  in rhombohedral phase [12]



## 15.2 Nanomechanics of Ferroelectric Thin Films

As all ferroelectric phase transitions are accompanied by a change in their prototypic crystal structure, the lattice parameters and phase stability in ferroelectrics could be drastically changed by external constraints. For example, when a ferroelectric thin film is constrained by a substrate (Fig. 15.2), the strains inside the film can significantly affect both the ferroelectric transition temperature and the domain configuration.

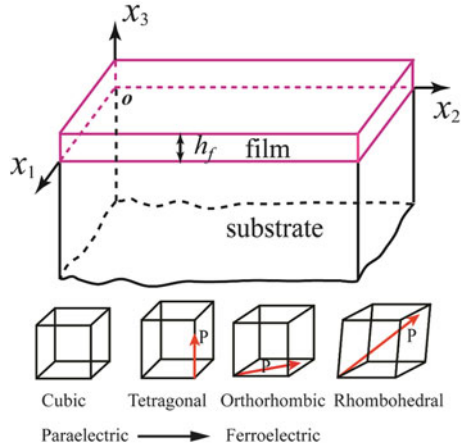
The structural changes associated with ferroelectric phase transition can be described by stress-free strains (also called eigenstrains or spontaneous strains)  $\varepsilon_{ij}^0$ . In rectangular coordinate  $\mathbf{x} = (x_1, x_2, x_3)$ , these strains are related to the polarization as:

$$\varepsilon_{ij}^0 = q_{ijkl} P_k P_l, \quad (15.2)$$

where  $q_{ijkl}$  are the electrostrictive coefficients, which are usually measured experimentally. For a cubic crystal material, Eq. (15.2) degenerates to

$$\begin{aligned} \varepsilon_{11}^0 &= Q_{11} P_1^2 + Q_{12} (P_2^2 + P_3^2), & \varepsilon_{22}^0 &= Q_{11} P_2^2 + Q_{12} (P_1^2 + P_3^2), \\ \varepsilon_{33}^0 &= Q_{11} P_3^2 + Q_{12} (P_1^2 + P_2^2), & \varepsilon_{23}^0 &= Q_{44} P_2 P_3, \varepsilon_{13}^0 = Q_{44} P_1 P_3, \varepsilon_{12}^0 = Q_{44} P_1 P_2, \end{aligned} \quad (15.3)$$

**Fig. 15.2** Schematic illustrations of a thin film coherently constrained by a very thick substrate and transition from paraelectric to ferroelectric with changes of polarization directions and crystal structures.  $h_f$  refers to the film thickness



where  $Q_{ij}$  are the electrostrictive coefficients in Voigt notation. If we assume that the interfaces between ferroelectric domains developed during a ferroelectric phase transition and that the interface between the film and the substrate are coherent, elastic strains  $e_{ij}$  will be generated during the phase transition in order to accommodate the structural changes. They are given by

$$e_{ij} = \varepsilon_{ij} - \varepsilon_{ij}^0, \quad i, j = 1, 2, 3, \tag{15.4}$$

where  $\varepsilon_{ij}$  are the total strains. The corresponding elastic strain energy density can be expressed as

$$f_{\text{elastic}}(P_i, \varepsilon_{ij}) = \frac{1}{2}c_{ijkl}e_{ij}e_{kl} = \frac{1}{2}c_{ijkl}(\varepsilon_{ij} - \varepsilon_{ij}^0)(\varepsilon_{kl} - \varepsilon_{kl}^0), \tag{15.5}$$

where  $c_{ijkl}$  is the elastic stiffness tensor. Summation convention for repeated indices is employed and Latin letters  $i, j, k, l$  take on values of 1,2,3. For a cubic anisotropic material, elastic strain energy density can be written as

$$\begin{aligned} f_{\text{elastic}} = & \frac{1}{2}C_{11} \left[ (\varepsilon_{11} - \varepsilon_{11}^0)^2 + (\varepsilon_{22} - \varepsilon_{22}^0)^2 + (\varepsilon_{33} - \varepsilon_{33}^0)^2 \right] \\ & + C_{12} \left[ (\varepsilon_{11} - \varepsilon_{11}^0)(\varepsilon_{22} - \varepsilon_{22}^0) + (\varepsilon_{22} - \varepsilon_{22}^0)(\varepsilon_{33} - \varepsilon_{33}^0) + (\varepsilon_{11} - \varepsilon_{11}^0)(\varepsilon_{33} - \varepsilon_{33}^0) \right] \\ & + 2C_{44} \left[ (\varepsilon_{12} - \varepsilon_{12}^0)^2 + (\varepsilon_{23} - \varepsilon_{23}^0)^2 + (\varepsilon_{13} - \varepsilon_{13}^0)^2 \right], \end{aligned} \tag{15.6}$$

where  $C_{11}$ ,  $C_{12}$ , and  $C_{44}$  are the elastic stiffness components in Voigt notation. By expanding Eq. (15.6), we have

$$\begin{aligned}
f_{\text{elastic}} = & \frac{1}{2}C_{11} (\varepsilon_{11}^2 + \varepsilon_{22}^2 + \varepsilon_{33}^2) + C_{12} (\varepsilon_{11}\varepsilon_{22} + \varepsilon_{22}\varepsilon_{33} + \varepsilon_{11}\varepsilon_{33}) + 2C_{44} (\varepsilon_{12}^2 + \varepsilon_{23}^2 + \varepsilon_{13}^2) \\
& + \beta_{11} (P_1^4 + P_2^4 + P_3^4) + \beta_{12} (P_1^2 P_2^2 + P_2^2 P_3^2 + P_1^2 P_3^2) \\
- & (\lambda_{11}\varepsilon_{11} + \lambda_{12}\varepsilon_{22} + \lambda_{12}\varepsilon_{33}) P_1^2 - (\lambda_{12}\varepsilon_{11} + \lambda_{11}\varepsilon_{22} + \lambda_{12}\varepsilon_{33}) P_2^2 - (\lambda_{12}\varepsilon_{11} + \lambda_{12}\varepsilon_{22} + \lambda_{11}\varepsilon_{33}) P_3^2 \\
& - 2\lambda_{44} (\varepsilon_{12}P_1P_2 + \varepsilon_{23}P_2P_3 + \varepsilon_{13}P_1P_3),
\end{aligned} \tag{15.7}$$

where,

$$\begin{aligned}
\beta_{11} &= \frac{1}{2}C_{11} (Q_{11}^2 + 2Q_{12}^2) + C_{12}Q_{12} (2Q_{11} + Q_{12}), \\
\beta_{12} &= C_{12} (Q_{11}^2 + 3Q_{12}^2 + 2Q_{11}Q_{12}) + C_{11}Q_{12} (2Q_{11} + Q_{12}) + 2C_{44}Q_{44}^2, \\
\lambda_{11} &= C_{11}Q_{11} + 2C_{12}Q_{12}, \quad \lambda_{12} = C_{11}Q_{12} + C_{12} (Q_{11} + Q_{12}), \quad \lambda_{44} = 2C_{44}Q_{44}.
\end{aligned} \tag{15.8}$$

It can be seen that the presence of the strains and the elastic energy alters the coefficients of the polarization polynomial of Eq. (15.1), thus changes both the Curie temperature and polarization direction as well as the relative volume fractions of different domains when multiple domains coexist.

In order to calculate the strain field in a constrained film, small strains are assumed such that linear elasticity can be employed. The associated stresses  $\sigma_{ij}$  obey the Hooke's law,

$$\sigma_{ij} = c_{ijkl}e_{kl} = c_{ijkl} (\varepsilon_{kl} - \varepsilon_{kl}^0). \tag{15.9}$$

For a cubic anisotropic material, the stresses can be expanded as

$$\begin{aligned}
\sigma_{11} &= C_{11} (\varepsilon_{11} - \varepsilon_{11}^0) + C_{12} (\varepsilon_{22} - \varepsilon_{22}^0) + C_{12} (\varepsilon_{33} - \varepsilon_{33}^0), \\
\sigma_{22} &= C_{12} (\varepsilon_{11} - \varepsilon_{11}^0) + C_{11} (\varepsilon_{22} - \varepsilon_{22}^0) + C_{12} (\varepsilon_{33} - \varepsilon_{33}^0), \\
\sigma_{33} &= C_{12} (\varepsilon_{11} - \varepsilon_{11}^0) + C_{12} (\varepsilon_{22} - \varepsilon_{22}^0) + C_{11} (\varepsilon_{33} - \varepsilon_{33}^0), \\
\sigma_{23} &= 2C_{44} (\varepsilon_{23} - \varepsilon_{23}^0), \quad \sigma_{13} = 2C_{44} (\varepsilon_{13} - \varepsilon_{13}^0), \quad \sigma_{12} = 2C_{44} (\varepsilon_{12} - \varepsilon_{12}^0).
\end{aligned} \tag{15.10}$$

The stresses satisfy mechanical equilibrium which can be expressed as

$$\sigma_{ij,j} = \partial\sigma_{ij}/\partial x_j = 0, \quad (i = 1, 2, 3), \tag{15.11}$$

in the absence of body forces. Moreover, these stresses are required to satisfy any appropriate traction boundary conditions imposed on the studied film. If we consider a film with a stress-free surface, this means

$$\sigma_{i3} |_{\text{film-surface: } x_3=h_f} = 0 \quad (i = 1, 2, 3), \tag{15.12}$$

when the  $x_3$ -axis is perpendicular to the film plane, as shown in Fig. 15.2.

If the thin film is coherent with the substrate, then the total strain field in the thin film is controlled by the thick substrate. For example, for a cubic substrate

of lattice parameter,  $a_s$ , and a thin film with a stress-free lattice parameter,  $a_f$ , the corresponding in-plane strains,  $\bar{\varepsilon}_{\alpha\beta}$  ( $\alpha, \beta = 1, 2$ ), are given by

$$\bar{\varepsilon}_{11} = \bar{\varepsilon}_{22} = \frac{a_s - a_f}{a_s} = e_0, \quad \bar{\varepsilon}_{12} = 0. \quad (15.13)$$

In the following we will show how to solve the strains and stresses as well as the elastic energy for a film containing different domain structures.

(1) Single tetragonal  $c$ -domain

When a ferroelectric film contains only a single tetragonal  $c$ -domain (a domain whose polarization is normal to the film), the polarization in such a case has the form  $\mathbf{P} = (0, 0, P_s)$ , where  $P_s$  is the value of the spontaneous polarization. The stress-free strain caused by the polarization is given by  $\varepsilon_{11}^0 = Q_{12}P_s^2$ ,  $\varepsilon_{22}^0 = Q_{12}P_s^2$ ,  $\varepsilon_{33}^0 = Q_{11}P_s^2$ ,  $\varepsilon_{23}^0 = 0$ ,  $\varepsilon_{13}^0 = 0$ ,  $\varepsilon_{12}^0 = 0$ .

Because it is a single domain film, the corresponding stresses and strains are constants over the whole film. Therefore, the mechanical equilibrium Eq. (15.11) is satisfied automatically. The boundary condition (15.12) at the film surface requires  $\sigma_{13} = 2C_{44}\varepsilon_{13} = 0$ ,  $\sigma_{23} = 2C_{44}\varepsilon_{23} = 0$ ,  $\sigma_{33} = C_{12}(\varepsilon_{11} - Q_{12}P_s^2) + C_{12}(\varepsilon_{22} - Q_{12}P_s^2) + C_{11}(\varepsilon_{33} - Q_{11}P_s^2) = 0$ , and the boundary condition (15.13) from the substrate makes  $\varepsilon_{12} = \bar{\varepsilon}_{12} = 0$  and  $\varepsilon_{11} = \varepsilon_{22} = \bar{\varepsilon}_{11} = \bar{\varepsilon}_{22} = e_0$ . Therefore, we have  $\varepsilon_{13} = 0$ ,  $\varepsilon_{23} = 0$ , and  $\varepsilon_{33} = \frac{(C_{11}Q_{11} + 2C_{12}Q_{12})P_s^2 - 2C_{12}e_0}{C_{11}}$ . Thus, the corresponding elastic energy density becomes

$$f_{\text{elastic}/c} = \frac{(C_{11} - C_{12})(C_{11} + 2C_{12})}{C_{11}}(e_0 - Q_{12}P_s^2)^2. \quad (15.14)$$

At given substrate constraint strain ( $e_0$ ) and temperature ( $T$ ), the value of the polarization ( $P_s$ ) can be obtained by minimizing the total energy of the film with respect to the polarization. The total energy density is the sum of the elastic energy in Eq. (15.14) and the bulk free energy density in Eq. (15.1) with  $P_1 = P_2 = 0$ ,  $P_3 = P_s$ , i.e.,

$$f_{c\text{-domain}}(P_s) = (\alpha_1 + a_3)P_s^2 + (\alpha_{11} + a_{33})P_s^4 + \alpha_{111}P_s^6 + \alpha_{1111}P_s^8 + a_0, \quad (15.15)$$

where,

$$a_3 = -\frac{2(C_{11} - C_{12})(C_{11} + 2C_{12})Q_{12}e_0}{C_{11}},$$

$$a_{33} = \frac{(C_{11} - C_{12})(C_{11} + 2C_{12})Q_{12}^2}{C_{11}}, \quad a_0 = \frac{(C_{11} - C_{12})(C_{11} + 2C_{12})e_0^2}{C_{11}}. \quad (15.16)$$

Therefore, the polarization,  $P_s$ , can be obtained by solving  $\partial f_{c\text{-domain}}(P_s) / \partial P_s$ .

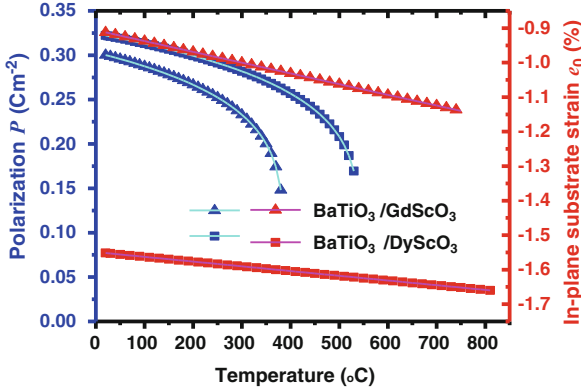


**Fig. 15.3** In-plane strain ( $e_0$ ) and polarization ( $P = P_s$ ) versus temperature in the (001) BaTiO<sub>3</sub> films commensurately grown on (110) GdScO<sub>3</sub> and DyScO<sub>3</sub> substrates, respectively

Experimentally, single crystal BaTiO<sub>3</sub> thin films were successfully grown on (110) GdScO<sub>3</sub> and (110) DyScO<sub>3</sub> single-crystal substrates by both reactive molecular beam epitaxy (MBE) and pulsed-laser deposition (PLD) with in situ high-pressure reflection high-energy electron diffraction [6]. These films are epitaxial, purely *c*-axis oriented, and fully coherent with the substrates without any resolvable lattice relaxation. The in-plane and out-of-plane lattice parameters of the films and substrates as a function of temperature were measured with a variable-temperature four-circle X-ray diffractometer equipped with a two-dimensional area detector with an angular resolution of  $\sim 0.02^\circ$ . From these measurements, the corresponding substrate constraint strain,  $e_0$ , is calculated and plotted in Fig. 15.3. For the constraint strain at the associated temperature, the corresponding spontaneous polarization can be calculated and is plotted in the same figure. In the calculations, the elastic constants and electrostrictive coefficients used were  $C_{11} = 1.78 \times 10^{11}$ ,  $C_{12} = 0.964 \times 10^{11}$ ,  $C_{44} = 1.22 \times 10^{11}$  (Nm<sup>-2</sup>),  $Q_{11} = 0.10$ ,  $Q_{12} = -0.034$ ,  $Q_{44} = 0.029$  (C<sup>-2</sup>m<sup>4</sup>) [7, 13–15], and the coefficients of Landau–Devonshire description of Eq. (15.1) were from Table 15.1. Comparing with the tetragonal phase in Fig. 15.1, both the ferroelectric transition temperature,  $T_c$ , and spontaneous polarization,  $P_s$ , changed significantly.

(2) Arbitrary single domain

For a film with a single phase of an arbitrary polarization  $\mathbf{P} = (P_1, P_2, P_3)$ , the film boundary conditions of Eqs. (15.12) and (15.13) yield:  $\varepsilon_{12} = 0$ ,  $\varepsilon_{11} = \varepsilon_{22} = e_0$ ,  $\varepsilon_{23} = Q_{44}P_2P_3$ ,  $\varepsilon_{13} = Q_{44}P_1P_3$ ,  $\varepsilon_{33} = \frac{C_{11}Q_{12} + C_{12}(Q_{11} + Q_{12})}{C_{11}}(P_1^2 + P_2^2) + \frac{(C_{11}Q_{11} + 2C_{12}Q_{12})}{C_{11}}P_3^2 - \frac{2C_{12}}{C_{11}}e_0$ . The corresponding elastic energy density is formulated as

$$f_{\text{elastic}/s} = a_0 + a_1(P_1^2 + P_2^2) + a_3P_3^2 + a_{11}(P_1^4 + P_2^4) + a_{33}P_3^4 + a_{12}P_1^2P_2^2 + a_{13}(P_1^2P_3^2 + P_2^2P_3^2), \quad (15.17)$$

with  $a_3$ ,  $a_{33}$ , and  $a_0$  given in Eq. (15.16), and

$$\begin{aligned}
 a_1 &= -\frac{(C_{11}-C_{12})(C_{11}+2C_{12})(Q_{11}+Q_{12})e_0}{C_{11}^2}, & a_{11} &= \frac{C_{11}^2(Q_{11}^2+Q_{12}^2)-C_{12}^2(Q_{11}+Q_{12})^2+2C_{11}C_{12}Q_{11}Q_{12}}{C_{11}^3}, \\
 a_{12} &= \frac{2C_{11}^2Q_{11}Q_{12}-C_{12}^2(Q_{11}+Q_{12})^2+C_{11}C_{12}(Q_{11}^2+Q_{12}^2)+2C_{11}C_{44}Q_{11}^2}{C_{11}^3}, \\
 a_{13} &= \frac{(C_{11}-C_{12})(C_{11}+2C_{12})Q_{12}(Q_{11}+Q_{12})}{C_{11}^3}.
 \end{aligned}
 \tag{15.18}$$

Obviously, with the addition of elastic energy of (15.17) into (15.1), the ferroelectric transition temperature and the polarization values and directions can be alerted notably when  $e_0$  is large [5]. However, some single phases with arbitrary polarizations cannot fully accommodate the equal biaxial stress. Nevertheless, single crystals with polarizations normal to the film can always accommodate any equal biaxial strain. Thus, if ferroelectrics are assumed to always form single domains, the results could be inaccurate resulting in incorrect predictions of phase diagrams of the ferroelectric material as a function of temperature and constraint strain [5].

(3) Twinned tetragonal domains

The phase transition from paraelectric to ferroelectric can lead to the formation of a twin domain structure, i.e., a structure consisting of two kinds of domains. In order to form a twin domain structure, the polarizations in the twin domains must have a specific relationship. For example, the tetragonal phase  $a_1 : (P_s, 0, 0)/a_2 : (0, P_s, 0)$  can form a twin structure as shown in Fig. 15.4. This twin domain structure has domain walls orthogonal to the film/substrate interface and orientated along the  $\{110\}$  planes of the prototypic cubic phase. The strain and stress distributions in the twin structure are calculated below.

In the twin structure shown in Fig. 15.4, the equilibrium volume fractions of  $a_1 : (P_s, 0, 0)$  and  $a_2 : (0, P_s, 0)$  are equal to each other and the spontaneous polarization  $P_s$  has the same magnitude in the two domains. The corresponding elastic energy density is calculated as

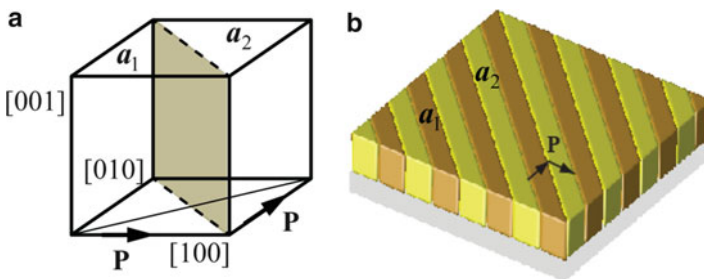


**Fig. 15.4** (a) Schematic illustration of a twin tetragonal  $a_1/a_2$  structure; (b) A domain structure of twinned  $a_1/a_2$  tetragonal phases obtained in a BaTiO<sub>3</sub> film



$$f_{\text{elastic}/a_1a_2} = \frac{1}{2}f_{\text{elastic}/a_1} + \frac{1}{2}f_{\text{elastic}/a_2}, \quad (15.19)$$

where the factor  $\frac{1}{2}$  represents the volume fraction of one of the twin domains.

In domain  $a_1 : (P_s, 0, 0)$ , the corresponding strains and stresses are  $\{\varepsilon_{11}^{a_1}, \varepsilon_{22}^{a_1}, \varepsilon_{33}^{a_1}, \varepsilon_{23}^{a_1}, \varepsilon_{13}^{a_1}, \varepsilon_{12}^{a_1}\}$  and  $\{\sigma_{11}^{a_1}, \sigma_{22}^{a_1}, \sigma_{33}^{a_1}, \sigma_{23}^{a_1}, \sigma_{13}^{a_1}, \sigma_{12}^{a_1}\}$ , respectively. In domain  $a_2 : (0, P_s, 0)$ , the corresponding strains and stresses are likewise  $\{\varepsilon_{11}^{a_2}, \varepsilon_{22}^{a_2}, \varepsilon_{33}^{a_2}, \varepsilon_{23}^{a_2}, \varepsilon_{13}^{a_2}, \varepsilon_{12}^{a_2}\}$  and  $\{\sigma_{11}^{a_2}, \sigma_{22}^{a_2}, \sigma_{33}^{a_2}, \sigma_{23}^{a_2}, \sigma_{13}^{a_2}, \sigma_{12}^{a_2}\}$ , respectively. They are required to satisfy the film surface boundary condition and substrate constraint conditions together. These conditions in the twinned structure are converted to

$$\frac{1}{2}\sigma_{33}^{a_1} + \frac{1}{2}\sigma_{33}^{a_2} = 0, \quad \frac{1}{2}\sigma_{13}^{a_1} + \frac{1}{2}\sigma_{13}^{a_2} = 0, \quad \frac{1}{2}\sigma_{23}^{a_1} + \frac{1}{2}\sigma_{23}^{a_2} = 0, \quad (15.20)$$

$$\frac{1}{2}\varepsilon_{11}^{a_1} + \frac{1}{2}\varepsilon_{11}^{a_2} = e_0, \quad \frac{1}{2}\varepsilon_{22}^{a_1} + \frac{1}{2}\varepsilon_{22}^{a_2} = e_0, \quad \frac{1}{2}\varepsilon_{12}^{a_1} + \frac{1}{2}\varepsilon_{12}^{a_2} = 0. \quad (15.21)$$

At the interface between the two domains, i.e., at the plane of (110) shown in Fig. 15.4a, the associated stresses and strains are continuous across the interface, i.e.,

$$\begin{aligned} \sigma_{11}^{a_1} + \sigma_{22}^{a_1} + 2\sigma_{12}^{a_1} &= \sigma_{11}^{a_2} + \sigma_{22}^{a_2} + 2\sigma_{12}^{a_2}, & \sigma_{11}^{a_1} - \sigma_{22}^{a_1} &= \sigma_{11}^{a_2} - \sigma_{22}^{a_2}, & \sigma_{13}^{a_1} + \sigma_{23}^{a_1} &= \sigma_{13}^{a_2} + \sigma_{23}^{a_2}, \\ \varepsilon_{33}^{a_1} &= \varepsilon_{33}^{a_2}, & \varepsilon_{11}^{a_1} + \varepsilon_{22}^{a_1} - 2\varepsilon_{12}^{a_1} &= \varepsilon_{11}^{a_2} + \varepsilon_{22}^{a_2} - 2\varepsilon_{12}^{a_2}, & \varepsilon_{23}^{a_1} - \varepsilon_{13}^{a_1} &= \varepsilon_{23}^{a_2} - \varepsilon_{13}^{a_2}. \end{aligned} \quad (15.22)$$

The stresses  $\sigma_{ij}^{a_1}$  and  $\sigma_{ij}^{a_2}$  are related to strains  $\varepsilon_{ij}^{a_1}$  and  $\varepsilon_{ij}^{a_2}$  through Eq. (15.10) in domains  $a_1$  and  $a_2$ , respectively, with  $\varepsilon_{11}^{0a_1} = Q_{11}P_s^2$ ,  $\varepsilon_{22}^{0a_1} = Q_{12}P_s^2$ ,  $\varepsilon_{33}^{0a_1} = Q_{12}P_s^2$ ,  $\varepsilon_{12}^{0a_1} = 0$ ,  $\varepsilon_{23}^{0a_1} = 0$ ,  $\varepsilon_{13}^{0a_1} = 0$ , and  $\varepsilon_{11}^{0a_2} = Q_{12}P_s^2$ ,  $\varepsilon_{22}^{0a_2} = Q_{11}P_s^2$ ,  $\varepsilon_{33}^{0a_2} = Q_{12}P_s^2$ ,  $\varepsilon_{12}^{0a_2} = 0$ ,  $\varepsilon_{23}^{0a_2} = 0$ ,  $\varepsilon_{13}^{0a_2} = 0$ . By solving Eqs. (15.20)–(15.22), we have  $\varepsilon_{11}^{a_1} = e_0 + \frac{1}{2}P_s^2(Q_{11} - Q_{12})$ ,  $\varepsilon_{22}^{a_1} = e_0 - \frac{1}{2}P_s^2(Q_{11} - Q_{12})$ ,  $\varepsilon_{33}^{a_1} = \frac{-2C_{12}e_0 + [C_{11}Q_{12} + C_{12}(Q_{11} + Q_{12})]P_s^2}{C_{11}}$ ,  $\varepsilon_{12}^{a_1} = 0$ ,  $\varepsilon_{13}^{a_1} = 0$ ,  $\varepsilon_{23}^{a_1} = 0$ ,  $\sigma_{11}^{a_1} = \sigma_{22}^{a_1} = \frac{(C_{11} - C_{12})(C_{11} + 2C_{12})[2e_0 - (Q_{11} + Q_{12})P_s^2]}{2C_{11}}$ ,  $\sigma_{33}^{a_1} = \sigma_{12}^{a_1} = \sigma_{13}^{a_1} = \sigma_{23}^{a_1} = 0$ , and  $\varepsilon_{11}^{a_2} = e_0 - \frac{1}{2}P_s^2(Q_{11} - Q_{12})$ ,  $\varepsilon_{22}^{a_2} = e_0 + \frac{1}{2}P_s^2(Q_{11} - Q_{12})$ ,  $\varepsilon_{33}^{a_2} = \frac{-2C_{12}e_0 + [C_{11}Q_{12} + C_{12}(Q_{11} + Q_{12})]P_s^2}{C_{11}}$ ,  $\varepsilon_{12}^{a_2} = 0$ ,  $\varepsilon_{13}^{a_2} = 0$ ,  $\varepsilon_{23}^{a_2} = 0$ ,  $\sigma_{11}^{a_2} = \sigma_{22}^{a_2} = \frac{(C_{11} - C_{12})(C_{11} + 2C_{12})[2e_0 - (Q_{11} + Q_{12})P_s^2]}{2C_{11}}$ ,  $\sigma_{33}^{a_2} = \sigma_{12}^{a_2} = \sigma_{13}^{a_2} = \sigma_{23}^{a_2} = 0$ . The corresponding elastic energy density is of the expression:

$$f_{\text{elastic}/a_1a_2} = \frac{(C_{11} - C_{12})(C_{11} + 2C_{12})[-2e_0 + P_s^2(Q_{11} + Q_{12})]^2}{4C_{11}}. \quad (15.23)$$

It will be seen later in Sect. 15.4 that such a tetragonal  $a_1 : (P_s, 0, 0)/a_2 : (0, P_s, 0)$  twin structure can be stabilized under tensile strain  $e_0$  at relative higher temperature.

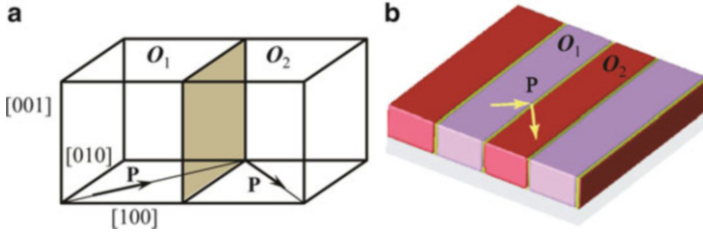


**Fig. 15.5** (a) Schematic illustration of a twin orthorhombic  $O_1/O_2$  structure; (b) A domain structure of twinned  $O_1/O_2$  orthorhombic phases obtained in a BaTiO<sub>3</sub> film

#### (4) Twinned orthorhombic domains

The twin structure shown in Fig. 15.5 also exists for the orthorhombic phases  $O_1 : (P_s/\sqrt{2}, P_s/\sqrt{2}, 0)$  and  $O_2 : (P_s/\sqrt{2}, -P_s/\sqrt{2}, 0)$ . This twinned structure has domain walls orthogonal to the film/substrate interface but orientated along the (100) or (010) planes of the prototypic cubic phase. In such a structure, the equilibrium volume fractions of  $O_1$ -domain and  $O_2$ -domain are also equal to each other and the spontaneous polarization  $P_s$  has the same magnitude in the two domains.

The corresponding elastic energy density can be evaluated by

$$f_{\text{elastic}/O_1O_2} = \frac{1}{2}f_{\text{elastic}/O_1} + \frac{1}{2}f_{\text{elastic}/O_2}. \quad (15.24)$$

In domain  $O_1 : (P_s/\sqrt{2}, P_s/\sqrt{2}, 0)$ , the corresponding strains and stresses are  $\{\varepsilon_{11}^{O_1}, \varepsilon_{22}^{O_1}, \varepsilon_{33}^{O_1}, \varepsilon_{23}^{O_1}, \varepsilon_{13}^{O_1}, \varepsilon_{12}^{O_1}\}$  and  $\{\sigma_{11}^{O_1}, \sigma_{22}^{O_1}, \sigma_{33}^{O_1}, \sigma_{23}^{O_1}, \sigma_{13}^{O_1}, \sigma_{12}^{O_1}\}$ , respectively. Similarly, in domain  $O_2 : (P_s/\sqrt{2}, -P_s/\sqrt{2}, 0)$ , the corresponding strains and stresses are  $\{\varepsilon_{11}^{O_2}, \varepsilon_{22}^{O_2}, \varepsilon_{33}^{O_2}, \varepsilon_{23}^{O_2}, \varepsilon_{13}^{O_2}, \varepsilon_{12}^{O_2}\}$  and  $\{\sigma_{11}^{O_2}, \sigma_{22}^{O_2}, \sigma_{33}^{O_2}, \sigma_{23}^{O_2}, \sigma_{13}^{O_2}, \sigma_{12}^{O_2}\}$ , respectively. They are required to satisfy the film surface stress-free boundary condition and substrate constraint condition:

$$\frac{1}{2}\sigma_{33}^{O_1} + \frac{1}{2}\sigma_{33}^{O_2} = 0, \quad \frac{1}{2}\sigma_{13}^{O_1} + \frac{1}{2}\sigma_{13}^{O_2} = 0, \quad \frac{1}{2}\sigma_{23}^{O_1} + \frac{1}{2}\sigma_{23}^{O_2} = 0, \quad (15.25)$$

$$\frac{1}{2}\varepsilon_{11}^{O_1} + \frac{1}{2}\varepsilon_{11}^{O_2} = e_0, \quad \frac{1}{2}\varepsilon_{22}^{O_1} + \frac{1}{2}\varepsilon_{22}^{O_2} = e_0, \quad \frac{1}{2}\varepsilon_{12}^{O_1} + \frac{1}{2}\varepsilon_{12}^{O_2} = 0. \quad (15.26)$$

At the interface between the two domains, the associated stresses and strains are required to be continuous, i.e.,

$$\sigma_{11}^{O_1} = \sigma_{11}^{O_2}, \quad \sigma_{12}^{O_1} = \sigma_{12}^{O_2}, \quad \sigma_{13}^{O_1} = \sigma_{13}^{O_2}, \quad \varepsilon_{22}^{O_1} = \varepsilon_{22}^{O_2}, \quad \varepsilon_{33}^{O_1} = \varepsilon_{33}^{O_2}, \quad \varepsilon_{23}^{O_1} = \varepsilon_{23}^{O_2}. \quad (15.27)$$

The solutions of Eqs. (15.25)–(15.27) are

$$\begin{aligned} \varepsilon_{11}^{O_1} = \varepsilon_{11}^{O_2} = e_0, \quad \varepsilon_{12}^{O_1} = -\varepsilon_{12}^{O_2} = \frac{1}{2} Q_{44} P_s^2, \quad \varepsilon_{13}^{O_1} = \varepsilon_{13}^{O_2} = 0, \\ \varepsilon_{23}^{O_1} = \varepsilon_{23}^{O_2} = 0, \quad \varepsilon_{22}^{O_1} = \varepsilon_{22}^{O_2} = e_0, \quad \varepsilon_{33}^{O_1} = \varepsilon_{33}^{O_2} = -\frac{C_{12}}{C_{11}} [2e_0 - (Q_{11} + Q_{12}) P_s^2] + Q_{12} P_s^2, \end{aligned} \quad (15.28)$$

since  $\varepsilon_{11}^{0O_1} = \frac{1}{2} (Q_{11} + Q_{12}) P_s^2$ ,  $\varepsilon_{22}^{0O_1} = \frac{1}{2} (Q_{11} + Q_{12}) P_s^2$ ,  $\varepsilon_{33}^{0O_1} = Q_{12} P_s^2$ ,  $\varepsilon_{23}^{0O_1} = 0$ ,  $\varepsilon_{13}^{0O_1} = 0$ ,  $\varepsilon_{12}^{0O_1} = \frac{1}{2} Q_{44} P_s^2$ , and  $\varepsilon_{11}^{0O_2} = \frac{1}{2} (Q_{11} + Q_{12}) P_s^2$ ,  $\varepsilon_{22}^{0O_2} = \frac{1}{2} (Q_{11} + Q_{12}) P_s^2$ ,  $\varepsilon_{33}^{0O_2} = Q_{12} P_s^2$ ,  $\varepsilon_{23}^{0O_2} = 0$ ,  $\varepsilon_{13}^{0O_2} = 0$ ,  $\varepsilon_{12}^{0O_2} = -\frac{1}{2} Q_{44} P_s^2$ . Therefore, we have

$$f_{\text{elastic}/O_1O_2} = \frac{(C_{11} - C_{12})(C_{11} + 2C_{12})}{4C_{11}} \left[ (Q_{11} + Q_{12})^2 P_s^4 - 4e_0 (Q_{11} + Q_{12}) P_s^2 + 4e_0^2 \right] \quad (15.29)$$

We will see later in Sect. 15.4 that such an orthorhombic  $O_1: (P_s/\sqrt{2}, P_s/\sqrt{2}, 0)$  and  $O_2: (P_s/\sqrt{2}, -P_s/\sqrt{2}, 0)$  twin structure can be stabilized under larger tensile strain  $e_0$  at quite a range of temperature down to 0 K.

In addition to the two kinds of twin domain structures discussed above, Koukhar et al. have considered more twin domain structures in their work [16]. It should be borne in mind, however, that not all these considered twin structures can completely accommodate with the equal biaxial in-plane constraint and not all domain walls lie along the  $\{100\}$  or  $\{110\}$  planes. For example, the twin domain structures, either  $c/a_1/$  or  $c/a_2/$ , cannot exist alone to accommodate the equal biaxial substrate constraint. Their combination, i.e.,  $c/a_1/a_2$  domain structures can be stabilized under certain constraints and temperatures. This will be seen from Sect. 15.4 of ferroelectric domain heterostructure.

#### (5) Heterostructure case

In the general case, the domain shapes and domain wall configurations in constrained films can be much more complicated than we have seen so far. For the general case, the internal strains and stresses cannot be solved analytically. They have to be solved numerically.

Consider a ferroelectric thin film grown on a substrate. Below the Curie temperature such that a ferroelectric transition occurs and a spontaneous polarization  $\mathbf{P} = (P_1, P_2, P_3)$  exists. However, the polarization is not homogeneous over the film but spatially dependent, i.e.,  $\mathbf{P}(\mathbf{x})$ . Since the proper ferroelectric phase transition involves structural change, a relation of Eqs. (15.2) or (15.3) between spontaneous or stress-free strains and spontaneous polarization is employed.

In order to consider the constraint strains on the ferroelectric film from its underlying substrate, the total strain of the film is separated into two parts. One part is a homogeneous strain  $\bar{\varepsilon}_{ij}$  that is the same for each point of the film. The other part is a heterogeneous strain,  $\eta_{ij}(\mathbf{x})$ . Therefore,

$$\varepsilon_{ij}(\mathbf{x}) = \bar{\varepsilon}_{ij} + \eta_{ij}(\mathbf{x}). \quad (15.30)$$

We let  $\bar{\varepsilon}_{\alpha\beta}$  ( $\alpha, \beta = 1, 2$ ) represent the macroscopic shape deformation of the film in the film plane. This means that  $\iiint_V \eta_{\alpha\beta}(\mathbf{x}) dV = 0$ , ( $\alpha, \beta = 1, 2$ ). For a thin film grown coherently on a thick substrate, the macroscopic deformation of the film in the film plane is totally controlled by the sufficiently thick substrate. Equation (15.13) gives the corresponding  $\bar{\varepsilon}_{\alpha\beta}$  ( $\alpha, \beta = 1, 2$ ) for the case of a film with cubic crystal structure grown coherently on a substrate of cubic crystal structure. The macroscopic deformation of the film along the  $x_3$  direction is determined by both the substrate constraint and the domain structure in the film. Since at film surface, the stress-free condition requires  $\sigma_{i3} \big|_{\text{film-surface: } x_3=h_f} = 0$ , i.e.,  $c_{i3kl}(\bar{\varepsilon}_{kl} + \eta_{kl} - \varepsilon_{kl}^0) \big|_{\text{film-surface: } x_3=h_f} = 0$ , we choose the quantity  $\bar{\varepsilon}_{i3}$  ( $i = 1, 2, 3$ ) in such a way that makes  $c_{i3kl}\bar{\varepsilon}_{kl} = 0$ . Then the stress-free of the film top surface becomes

$$c_{i3kl}(\eta_{kl} - \varepsilon_{kl}^0) \big|_{\text{film-surface: } x_3=h_f} = 0. \quad (15.31)$$

However, it needs to be pointed out that  $\bar{\varepsilon}_{i3}$  ( $i = 1, 2, 3$ ) employed here is only part of the total deformation of the film.

Assuming that the displacement  $u_i(\mathbf{x})$  is associated with the heterogeneous strain,  $\eta_{ij}(\mathbf{x})$ , i.e.,

$$\eta_{ij}(\mathbf{x}) = \frac{1}{2} [u_{i,j}(\mathbf{x}) + u_{j,i}(\mathbf{x})], \quad (15.32)$$

the mechanical equilibrium equations can be rewritten as

$$c_{ijkl}u_{k,lj}(\mathbf{x}) = c_{ijkl}\varepsilon_{kl,j}^0(\mathbf{x}). \quad (15.33)$$

And the film surface stress-free condition becomes

$$c_{i3kl}(u_{k,l} - \varepsilon_{kl}^0) \big|_{\text{film-surface: } x_3=h_f} = 0. \quad (15.34)$$

Because the elastic perturbation resulting from the heterogeneous strain disappears in the substrate far away from the film-substrate interface, one can use the following condition:

$$u_i \big|_{x_3=-h_s} = 0 \quad (15.35)$$

to replace the constraint of the substrate. In the equation,  $h_s$  is the distance from the film-substrate interface into the substrate, beyond which the elastic deformation is ignored. Actually it was verified numerically that the domain shapes practically do not change when  $h_s$  exceeds about half of the film thickness [17].

After solving Eq. (15.33) under boundary conditions (15.34) and (15.35) with given polarization distribution, the strain field  $\varepsilon_{ij}(\mathbf{x})$  can be calculated from Eqs. (15.30) and (15.32). For the sake of simplicity, the elastic properties of the film and the substrate are assumed to be the same although the elastic anisotropy can be arbitrary. An efficient and accurate numerical method was proposed to solve  $u_i(\mathbf{x})$  from Eqs. (15.33)–(15.35) [17]. It converts a three-dimensional (3D) problem into an out-of-plane one-dimensional (1D) problem by using the fast Fourier transformation (FFT) and gives an analytical solution along the out-of-plane direction. Thus the obtained solution is a semi-analytical solution which satisfies the boundary condition (15.34) and (15.35) analytically.

Figure 15.6a illustrates the distribution of the displacement component  $u_3(\mathbf{x})$  on the top surface of a film with a given domain structure of Fig. 15.6b. The domain structure of Fig. 15.6b is from a phase field simulation [17]. The displacements were the solution of Eqs. (15.33)–(15.35) with the given domain structure, i.e., the distribution of  $P_i(\mathbf{x})$  ( $i = 1, 2, 3$ ). This shows that the wrinkly surface reflects the domain morphology of the film. Since ferroelectric domain sizes are on the order of nanometers, the displacements at the thin film free surface are also on the order of nanometers or less.

### 15.3 Phase Field Method

To investigate the stability of ferroelectric phases and the details of the associated ferroelectric domain structure in a thin film constrained by its underlying substrate, the phase field method (PFM) is widely used [17–36] and is reviewed in detail by Chen [37]. The PFM for ferroelectrics is based on the Landau–Devonshire theory of phase transition and searched for the minimum energy state of the system using the time-dependent Ginzburg–Landau (TDGL) evolution equation. The TDGL

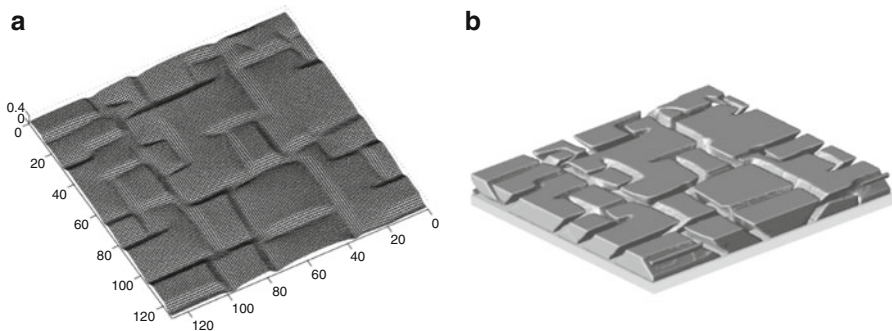


**Fig. 15.6** (a) Displacement pattern of the  $x_3$  component  $u_3$  on the surface of the ferroelectric film with domain structure of (b). In (b), the solid areas are tetragonal  $c$ -domains and the open areas are tetragonal  $a_1/a_2$ -domains [17]

equations in terms of the polarization components  $P_i(\mathbf{x})$  are

$$\frac{\partial P_i(\mathbf{x}, t)}{\partial t} = -L \frac{\delta F}{\delta P_i(\mathbf{x}, t)}, \quad (i = 1, 2, 3), \quad (15.36)$$

where  $L$  is the kinetic coefficient, and  $F$  is the total free energy of the system.  $\delta F/\delta P_i(\mathbf{x}, t)$  is the thermodynamic driving force for the spatial and temporal evolution of  $P_i(\mathbf{x}, t)$ . The total free energy of the system includes bulk free energy, elastic energy, domain wall energy, and the depolarization energy. In order to distinguish the impact of the substrate mechanical constraint on the domain structures of the film, the depolarization energy considered in Ref. [19] is neglected here. Therefore, the total energy is

$$F = \iiint_V [f_{\text{bulk}} + f_{\text{elastic}} + f_{\text{wall}}] dV, \quad (15.37)$$

where the densities of bulk free energy and elastic energy are given in Eqs. (15.1) and (15.5), respectively.

The domain wall energy is evaluated through the gradients of the polarization field. For a general anisotropic system, the gradient energy density may be calculated by

$$f_{\text{wall}} = \frac{1}{2} g_{ijkl} P_{ij} P_{kl}, \quad (15.38)$$

where  $P_{ij} = \partial P_i / \partial x_j$  and  $g_{ijkl}$  are the gradient energy coefficients with the property of  $g_{ijkl} = g_{klij}$ . For a cubic system, this degenerates into

$$\begin{aligned} f_{\text{wall}} = & \frac{1}{2} G_{11} (P_{1,1}^2 + P_{2,2}^2 + P_{3,3}^2) + G_{12} (P_{1,1}P_{2,2} + P_{2,2}^2P_{3,3}^2 + P_{1,1}P_{3,3}) \\ & + \frac{1}{2} G_{44} [(P_{1,2} + P_{2,1})^2 + (P_{2,3} + P_{3,2})^2 + (P_{1,3} + P_{3,1})^2] \\ & + \frac{1}{2} G'_{44} [(P_{1,2} - P_{2,1})^2 + (P_{2,3} - P_{3,2})^2 + (P_{1,3} - P_{3,1})^2], \end{aligned} \quad (15.39)$$

where  $G_{ij}$  are also called as the gradient energy coefficients and are related to  $g_{ijkl}$  through Voigt notation, for instance,  $G_{11} = g_{1111}$ .

The temporal evolution of the polarization fields is obtained by numerically solving the TDGL Eq. (15.36). The semi-implicit Fourier spectral method for the time-stepping and spatial discretization proposed in Ref. [38] gives more efficient and accurate numerical solution for Eq. (15.36) so is recommended. Since the strains,  $\varepsilon_{ij}(\mathbf{x})$ , as well as the displacements,  $u_i(\mathbf{x})$ , are coupled with polarization components,  $P_i(\mathbf{x})$ , Eqs. (15.33)–(15.36) are solved iteratively. Once we have solutions for the polarization components, their spatial distribution gives the detail of a ferroelectric domain structure.

## 15.4 Ferroelectric Domain Heterostructure

The ferroelectric domain structure in the film can be obtained by solving the TDLG Eq. (15.36) and its coupling mechanical Eqs. (15.33)–(15.35) for a given temperature ( $T$ ) and mismatch strain ( $e_0$ ). Figure 15.7 illustrates some ferroelectric domain structures obtained through solving Eqs. (15.33)–(15.36) for BaTiO<sub>3</sub> films. All the data points shown in Fig. 15.7 were obtained by starting from an initial paraelectric state with small random perturbations. The data points simply represent the type of domain structures that exist at the end of a sufficiently long simulation for minimizing the total free energy. The various ferroelectric phases were determined by the non-zero components of local polarization.

In obtaining the domain structures of Fig. 15.7, a model size of  $128\Delta x \times 128\Delta x \times 36\Delta x$  cubic grids was employed and periodic boundary conditions were applied along the  $x_1$  and  $x_2$  axes. The thickness of the film is  $h_f = 20\Delta x$  so  $\mathbf{P}(x_1, x_2, x_3 > h_f) = 0$  is assumed. The region of the substrate allowed to deform was set to be  $h_s = 12\Delta x$  as it was pointed out previously that little change in results when  $h_s$  exceeds about half of the film thickness. Isotropic domain wall energy was assumed in Eq. (15.39) where  $G_{44} = G'_{44} = G_{11}/2$ , and  $G_{12} = 0$ .  $\Delta x = \sqrt{G_{11}/\alpha_0}$  and  $\Delta t = 1/(\alpha_0 L)$  with  $\alpha_0 = |\alpha_1|_{T=25^\circ\text{C}}$  were utilized for the normalization of Eq. (15.36).

It should be pointed out that the phase field simulations do not assume the domain wall orientations a priori. All the stable phases and domain structure that were determined under given temperature and substrate constraint strain were found

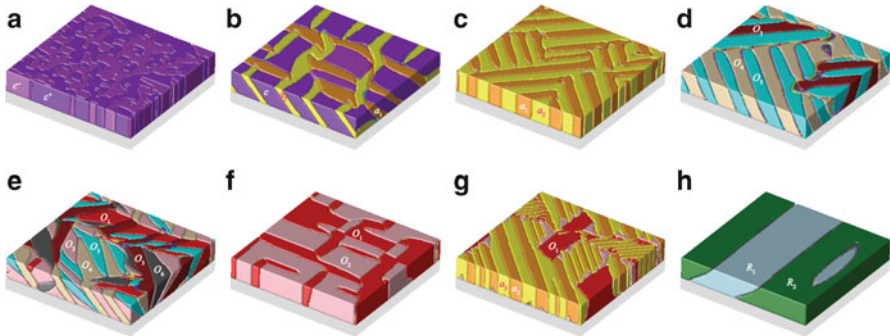


**Fig. 15.7** Domain morphologies in BaTiO<sub>3</sub> films as a function of temperature ( $T$ ) and substrate constraint strain ( $e_0$ ). Domain definitions and the corresponding polarizations:  $a_1: (P_1, 0, 0)$ ;  $a_2: (0, P_1, 0)$ ;  $c: (0, 0, P_3)$ ;  $O_1: (P_1, P_1, 0)$ ;  $O_2: (P_1, -P_1, 0)$ ;  $O_3: (P_1, 0, P_3)$ ;  $O_4: (P_1, 0, -P_3)$ ;  $O_5: (0, P_1, P_3)$ ;  $O_6: (0, P_1, -P_3)$ ;  $R_1: (-P_1, -P_1, P_3)$ ;  $R_2: (P_1, -P_1, P_3)$ . (a) tetragonal  $c$ -phase at  $T = 25^\circ\text{C}$  and  $e_0 = -1.0\%$ ; (b) tetragonal  $c$ -phase and  $a_1/a_2$ -phases at  $T = 75^\circ\text{C}$  and  $e_0 = 0.0$ ; (c) tetragonal  $a_1/a_2$ -phases at  $T = 75^\circ\text{C}$  and  $e_0 = 0.0$ ; (d) phases  $O_3/O_4/O_5$  at  $T = -25^\circ\text{C}$  and  $e_0 = -0.05\%$ ; (e) phases  $O_1/O_2/O_3/O_4/O_5/O_6$  at  $T = -25^\circ\text{C}$  and  $e_0 = 0.1\%$ ; (f) phases  $O_1/O_2$  at  $T = 25^\circ\text{C}$  and  $e_0 = 1.0\%$ ; (g) phases  $a_1/a_2/O_1/O_2$  at  $T = 25^\circ\text{C}$  and  $e_0 = 0.25\%$ ; (h) phases  $R_1/R_2$  at  $T = -100^\circ\text{C}$  and  $e_0 = 0.1\%$  [7]

from the minimization of total energy, i.e., the TDLG Eq. (15.36). These solutions were found by assigning small random numbers for  $P_i(\mathbf{x})$  at beginning to represent an initial paraelectric state. It is seen that under larger tensile strains that the polarization of ferroelectric phases is parallel to the film/substrate interface, either along  $\langle 100 \rangle$  or  $\langle 110 \rangle$  direction depending on the temperature and the magnitude of the strain. The corresponding domain structures are similar to either the  $a_1/a_2$  twins as shown in Fig. 15.7c, or the  $O_1/O_2$  twins of Fig. 15.7f, or the mixture of  $a_1/a_2$  twins and  $O_1/O_2$  twins shown in Fig. 15.7g. Under relative smaller strains the polarization changes its orientation from  $\langle 100 \rangle$  to  $\langle 10\gamma \rangle$  then to  $\langle 11\gamma \rangle$  as temperature decreases. This sequence is similar to that in bulk single crystals but  $\gamma$  is not always equal to 1 as in the bulk. The domain variants vary with the in-plane strain,  $e_0$ , which is clearly shown in Fig. 15.7a–c for the  $\langle 100 \rangle$  orientated polarizations and in Fig. 15.7d–f for the  $\langle 10\gamma \rangle$  orientated polarizations. It is interesting to note that the domain structures with  $\langle 10\gamma \rangle$  orientated polarizations can be rather complicated: the domain walls between different variants are not only along the  $\{100\}$  and  $\{110\}$  planes, i.e., the crystallographically prominent walls with a fixed orientation, but also along the so-called S-walls whose orientations depend on the magnitude of the polarization, electrostrictive coefficients, and substrate constraint [39]. When the strain is small, its effect on the orientation of orthorhombic domain walls can be ignored. In such a case, the permissible domain walls are either  $\{100\}$  or  $\{110\}$  or  $\{11\gamma\}$  planes with  $\gamma = 2Q_{44}/(Q_{11} - Q_{12}) = 0.4403$ .

Based on the simulation results, a phase diagram, i.e., a representation of stable ferroelectric phases and domain structures as a function of temperature and strain, was constructed and is shown in Fig. 15.8. Under sufficiently large compressive strains, the ferroelectric phase is of tetragonal symmetry with polarization orthogonal to the film/substrate interface. Figure 15.7a is a typical domain structure under large compressive strains, in which there are two types of  $c$ -domains separated by  $180^\circ$  domain walls. This result has been confirmed by experimental measurements on  $\text{BaTiO}_3$  films commensurately grown on  $\text{DyScO}_3$  and  $\text{GdScO}_3$  substrates through reactive MBE and PLD, respectively [6]. Under sufficiently large tensile strains, the ferroelectric phase is of orthorhombic symmetry with polarization parallel to the film/substrate interface. Figure 15.7f is a typical domain structure under large tensile strains. It is seen that from the phase diagram that under certain ranges of strains, the ferroelectric phases with both symmetries  $P4mm$  and  $Bmm2$  can be stable down all the way to 0 K without further transformation.

## 15.5 Summary

In summary, ferroelectrics and nanomechanics are coupled. Ferroelectric transitions involve material crystal structure change. The domain structure in ferroelectric films organizes or forms in a way to reduce the total free energy of the system and accommodate the constraint imposed on the film by its underlying substrate. On the other hand, the film ferroelectric properties are determined by its domain structure.



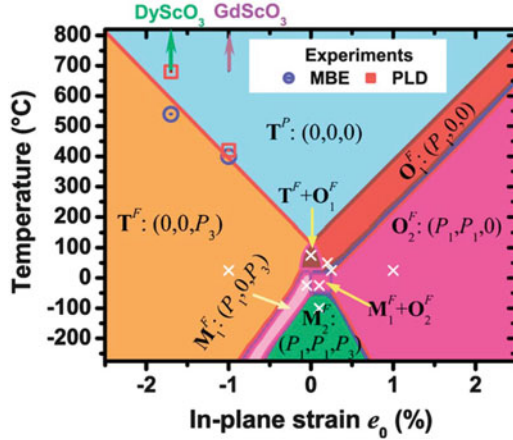


**Fig. 15.8** Phase diagram of BaTiO<sub>3</sub> films as a function of temperature and substrate in-plane strain. The scattered circles and squares denote the ferroelectric transition temperatures measured from experiments on the BaTiO<sub>3</sub> films commensurately grown on DyScO<sub>3</sub> and GdScO<sub>3</sub> substrates, respectively [6]. The “x” indicates the locations of the domain structures shown in Fig. 15.7. Each single phase has equivalent variants with polarization vectors of  $\mathbf{P} = (0, 0, 0)$  in  $T^P$ ;  $\mathbf{P} = (0, 0, \pm P_3)$  in  $T^F$ ;  $\mathbf{P} = (\pm P_1, 0, 0)/\mathbf{P} = (0, \pm P_1, 0)$  in  $O_1^F$ ;  $\mathbf{P} = (\pm P_1, \pm P_1, 0)/(\pm P_1, \mp P_1, 0)$  in  $O_2^F$ ;  $\mathbf{P} = (\pm P_1, 0, \pm P_3)/(\pm P_1, 0, \mp P_3)/(0, \pm P_1, \pm P_3)/(0, \pm P_1, \mp P_3)$  in  $M_1^F$ ;  $\mathbf{P} = (\pm P_1, \pm P_1, \pm P_3)/(\pm P_1, \mp P_1, \pm P_3)/(\pm P_1, \pm P_1, \mp P_3)/(\pm P_1, \mp P_1, \mp P_3)$  in  $M_2^F$  [7]

Therefore, this coupling can be used to engineer ferroelectric material properties. Such applications can be found in Refs. [6, 40–43].

This chapter presented methods for calculating strains and stresses in ferroelectric thin films containing nanoscale heterogeneous domain structures. The effect of strains on the ferroelectric transition temperature, stability of ferroelectric phases, and the domain structure were demonstrated for BaTiO<sub>3</sub> films. The PFM has been proven a powerful numerical method in predicting the effect of substrate constraint on the phase transitions and the details of domain structures in ferroelectrics without any priori assumptions on the possible domain structure. In addition to BaTiO<sub>3</sub> films, phase field simulations have been applied to predicting ferroelectric heterogeneous domain structures in PbTiO<sub>3</sub> [17–19, 32, 44], PZT [21, 45–47], SrTiO<sub>3</sub> [48], BiFeO<sub>3</sub> [49, 50], and SrBi<sub>2</sub>Nb<sub>2</sub>O<sub>9</sub> [51] thin films and BaTiO<sub>3</sub>/SrTiO<sub>3</sub> [52, 53], PZT/PZT [36], PbTiO<sub>3</sub>/BaTiO<sub>3</sub> [54, 55] superlattices. In calculating strain/stress distribution in thin films, homogeneous elastic properties in both the film and the substrate were assumed in order to use a semi-analytical solution for numerical accuracy and efficiency. This limitation, however, can be removed by utilizing an efficient iteration method proposed by Hu and Chen [56]. If one uses the concept of eigenstrains or stress-free strains, it is possible to consider the effect of any arbitrary distribution of dislocations and defects on microstructure evolution [57]. Very recently, efficient numerical methods for solving finite/large deformation have been developed [58–60]. Unlike small deformation, the large

deformation causes large strain gradient and/or localized deformation, which may affect phase transition kinetics including second phase nucleation and transition sequence, hence, the microstructure, material property, and response. With these methods, the phase field model presented in this chapter can be extended to take large deformation into account in ferroelectric phase transition.

## References

1. J. Valasek, Piezoelectric and allied phenomena in Rochelle salt. *Phys. Rev.* **15**, 537–538 (1920)
2. H.F. Kay, P. Vousden, Symmetry changes in barium titanate at low temperatures and their relation to its ferroelectric properties. *Philos. Mag.* **40**, 1019–1040 (1949)
3. W.J. Merz, The electric and optical behavior of BaTiO<sub>3</sub> single-domain crystals. *Phys. Rev.* **76**, 1221–1225 (1949)
4. Y. Yoneda, T. Okabe, K. Sakaue, H. Terauchi, H. Kasatani, K. Deguchi, Structural characterization of BaTiO<sub>3</sub> thin films grown by molecular beam epitaxy. *J. Appl. Phys.* **83**, 2458–2461 (1998)
5. N.A. Pertsev, A.G. Zembilgotov, A.K. Tagantsev, Effect of mechanical boundary conditions on phase diagrams of epitaxial ferroelectric thin films. *Phys. Rev. Lett.* **80**, 1988–1991 (1998)
6. K.J. Choi, M. Biegalski, Y.L. Li, A. Sharan, J. Schubert, R. Uecker, P. Reiche, Y.B. Chen, X.Q. Pan, V. Gopalan, L.Q. Chen, D.G. Schlom, C.B. Eom, Enhancement of ferroelectricity in strained BaTiO<sub>3</sub> thin films. *Science* **306**, 1005–1009 (2004)
7. Y.L. Li, L.Q. Chen, Temperature-strain phase diagram for BaTiO<sub>3</sub> thin films. *Appl. Phys. Lett.* **88**, 072905 (2006)
8. D.A. Tenne, X.X. Xi, Y.L. Li, L.Q. Chen, A. Soukiassian, M.H. Zhu, A.R. James, J. Lettieri, D.G. Schlom, W. Tian, X.Q. Pan, Absence of low-temperature phase transitions in epitaxial BaTiO<sub>3</sub> thin films. *Phys. Rev. B* **69**, 174101 (2004)
9. A.F. Devonshire, Theory of ferroelectrics. *Adv. Phys.* **3**, 85–130 (1954)
10. A.F. Devonshire, Theory of barium titanate 1. *Philos. Mag.* **40**, 1040–1063 (1949)
11. F. Jona, G. Shirane, *Ferroelectric Crystals* (Pergamon, Oxford, New York, 1962)
12. Y.L. Li, L.E. Cross, L.Q. Chen, A phenomenological thermodynamic potential for BaTiO<sub>3</sub> single crystals. *J. Appl. Phys.* **98**, 064101 (2005)
13. A.F. Devonshire, Theory of barium titanate 2. *Philos. Mag.* **42**, 1065–1079 (1951)
14. D. Berlincourt, H. Jaffe, Elastic and piezoelectric coefficients of single-crystal barium titanate. *Phys. Rev.* **111**, 143–148 (1958)
15. T. Yamada, Electromechanical properties of oxygen-octahedra ferroelectric crystals. *J. Appl. Phys.* **43**, 328–338 (1972)
16. V.G. Koukhar, N.A. Pertsev, R. Waser, Thermodynamic theory of epitaxial ferroelectric thin films with dense domain structures. *Phys. Rev. B* **64**, 214103 (2001)
17. Y.L. Li, S.Y. Hu, Z.K. Liu, L.Q. Chen, Effect of substrate constraint on the stability and evolution of ferroelectric domain structures in thin films. *Acta Mater.* **50**, 395–411 (2002)
18. Y.L. Li, S.Y. Hu, Z.K. Liu, L.Q. Chen, Phase-field model of domain structures in ferroelectric thin films. *Appl. Phys. Lett.* **78**, 3878–3880 (2001)
19. Y.L. Li, S.Y. Hu, Z.K. Liu, L.Q. Chen, Effect of electrical boundary conditions on ferroelectric domain structures in thin films. *Appl. Phys. Lett.* **81**, 427–429 (2002)
20. L.Q. Chen, Phase-field models for microstructure evolution. *Annu. Rev. Mater. Res.* **32**, 113–140 (2002)
21. Y.L. Li, S. Choudhury, Z.K. Liu, L.Q. Chen, Effect of external mechanical constraints on the phase diagram of epitaxial PbZr<sub>1-x</sub>Ti<sub>x</sub>O<sub>3</sub> thin films: thermodynamic calculations and phase-field simulations. *Appl. Phys. Lett.* **83**, 1608–1610 (2003)

22. A. Artemev, Phase field modeling of domain structures and  $P$ - $E$  hysteresis in thin ferroelectric layers with deadlayers. *Philos. Mag.* **90**, 89–101 (2010)
23. A. Artemev, B. Geddes, J. Slutsker, A. Roytburd, Thermodynamic analysis and phase field modeling of domain structures in bilayer ferroelectric thin films. *J. Appl. Phys.* **103**, 074104 (2008)
24. W.J. Chen, Y. Zheng, B. Wang, Phase field simulations of stress controlling the vortex domain structures in ferroelectric nanosheets. *Appl. Phys. Lett.* **100**, 062901 (2012)
25. P. Chu, D.P. Chen, J.M. Liu, Multiferroic domain structure in orthorhombic multiferroics of cycloidal spin order: phase field simulations. *Appl. Phys. Lett.* **101**, 042908 (2012)
26. K. Dayal, K. Bhattacharya, A real-space non-local phase-field model of ferroelectric domain patterns in complex geometries. *Acta Mater.* **55**, 1907–1917 (2007)
27. W.D. Dong, D.M. Pisani, C.S. Lynch, A finite element based phase field model for ferroelectric domain evolution. *Smart Mater. Struct.* **21**, 094014 (2012)
28. C. Fang, Phase-field simulation study on size effect of the microstructure evolution of a single-domain barium titanate 2D lattice square. *Phys. Status Solidi B* **251**, 1619–1629 (2014)
29. T. Koyama, H. Onodera, Phase-field simulation of ferroelectric domain microstructure changes in  $\text{BaTiO}_3$ . *Mater. Trans.* **50**, 970–976 (2009)
30. P.L. Liu, J. Wang, T.Y. Zhang, Y. Li, L.Q. Chen, X.Q. Ma, W.Y. Chu, L.J. Qiao, Effects of unequally biaxial misfit strains on polarization phase diagrams in embedded ferroelectric thin layers: phase field simulations. *Appl. Phys. Lett.* **93**, 132908 (2008)
31. D.C. Ma, Y. Zheng, C.H. Woo, Phase-field simulation of domain structure for  $\text{PbTiO}_3/\text{SrTiO}_3$  superlattices. *Acta Mater.* **57**, 4736–4744 (2009)
32. G. Sheng, J.X. Zhang, Y.L. Li, S. Choudhury, Q.X. Jia, Z.K. Liu, L.Q. Chen, Domain stability of  $\text{PbTiO}_3$  thin films under anisotropic misfit strains: phase-field simulations. *J. Appl. Phys.* **104**, 054105 (2008)
33. Y. Shindo, F. Narita, T. Kobayashi, Phase field simulation on the electromechanical response of poled barium titanate polycrystals with oxygen vacancies. *J. Appl. Phys.* **117**, 234103 (2015)
34. B. Winchester, P. Wu, L.Q. Chen, Phase-field simulation of domain structures in epitaxial  $\text{BiFeO}_3$  films on vicinal substrates. *Appl. Phys. Lett.* **99**, 052903 (2011)
35. P.P. Wu, X.Q. Ma, J.X. Zhang, L.Q. Chen, Phase-field model of multiferroic composites: domain structures of ferroelectric particles embedded in a ferromagnetic matrix. *Philos. Mag.* **90**, 125–140 (2010)
36. F. Xue, J.J. Wang, G. Sheng, E. Huang, Y. Cao, H.H. Huang, P. Munroe, R. Mahjoub, Y.L. Li, V. Nagarajan, L.Q. Chen, Phase field simulations of ferroelectrics domain structures in  $\text{PbZr}_x\text{Ti}_{1-x}\text{O}_3$  bilayers. *Acta Mater.* **61**, 2909–2918 (2013)
37. L.-Q. Chen, Phase-field method of phase transitions/domain structures in ferroelectric thin films: a review. *J. Am. Ceram. Soc.* **91**, 1835–1844 (2008)
38. L.Q. Chen, J. Shen, Applications of semi-implicit Fourier-spectral method to phase field equations. *Comput. Phys. Commun.* **108**, 147–158 (1998)
39. J. Fousek, V. Janovec, Orientation of domain walls in twinned ferroelectric crystals. *J. Appl. Phys.* **40**, 135–142 (1969)
40. J.H. Haeni, P. Irvin, W. Chang, R. Uecker, P. Reiche, Y.L. Li, S. Choudhury, W. Tian, M.E. Hawley, B. Craigo, A.K. Tagantsev, X.Q. Pan, S.K. Streiffer, L.Q. Chen, S.W. Kirchoefer, J. Levy, D.G. Schlom, Room-temperature ferroelectricity in strained  $\text{SrTiO}_3$ . *Nature* **430**, 758–761 (2004)
41. D.A. Tenne, A. Bruchhausen, N.D. Lanzillotti-Kimura, A. Fainstein, R.S. Katiyar, A. Cantarero, A. Soukiasian, V. Vaithyanathan, J.H. Haeni, W. Tian, D.G. Schlom, K.J. Choi, D.M. Kim, C.B. Eom, H.P. Sun, X.Q. Pan, Y.L. Li, L.Q. Chen, Q.X. Jia, S.M. Nakhmanson, K.M. Rabe, X.X. Xi, Probing nanoscale ferroelectricity by ultraviolet Raman spectroscopy. *Science* **313**, 1614–1616 (2006)
42. D.G. Schlom, L.-Q. Chen, C.-B. Eom, K.M. Rabe, S.K. Streiffer, J.-M. Triscone, Strain tuning of ferroelectric thin films. *Annu. Rev. Mater. Res.* **37**, 589–626 (2007)
43. D.G. Schlom, L.-Q. Chen, C.J. Fennie, V. Gopalan, D.A. Muller, X. Pan, R. Ramesh, R. Uecker, Elastic strain engineering of ferroic oxides. *MRS Bull.* **39**, 118–130 (2014)

44. G. Sheng, J.M. Hu, J.X. Zhang, Y.L. Li, Z.K. Liu, L.Q. Chen, Phase-field simulations of thickness-dependent domain stability in  $\text{PbTiO}_3$  thin films. *Acta Mater.* **60**, 3296–3301 (2012)
45. Y.L. Li, S.Y. Hu, L.Q. Chen, Ferroelectric domain morphologies of (001)  $\text{PbZr}_{1-x}\text{Ti}_x\text{O}_3$  epitaxial thin films. *J. Appl. Phys.* **97**, 034112 (2005)
46. Y. Cao, G. Sheng, J.X. Zhang, S. Choudhury, Y.L. Li, C.A. Randall, L.Q. Chen, Piezoelectric response of single-crystal  $\text{PbZr}_{1-x}\text{Ti}_x\text{O}_3$  near morphotropic phase boundary predicted by phase-field simulation. *Appl. Phys. Lett.* **97**, 252904 (2010)
47. S. Choudhury, Y.L. Li, L.Q. Chen, A phase diagram for epitaxial  $\text{PbZr}_{1-x}\text{Ti}_x\text{O}_3$  thin films at the bulk morphotropic boundary composition. *J. Am. Ceram. Soc.* **88**, 1669–1672 (2005)
48. Y.L. Li, S. Choudhury, J.H. Haeni, M.D. Biegalski, A. Vasudevarao, A. Sharan, H.Z. Ma, J. Levy, V. Gopalan, S. Trolier-McKinstry, D.G. Schlom, Q.X. Jia, L.Q. Chen, Phase transitions and domain structures in strained pseudocubic (100)  $\text{SrTiO}_3$  thin films. *Phys. Rev. B* **73**, 184112 (2006)
49. J.X. Zhang, Y.L. Li, S. Choudhury, L.Q. Chen, Y.H. Chu, F. Zavaliche, M.P. Cruz, R. Ramesh, Q.X. Jia, Computer simulation of ferroelectric domain structures in epitaxial  $\text{BiFeO}_3$  thin films. *J. Appl. Phys.* **103**, 094111 (2008)
50. J.X. Zhang, Y.L. Li, Y. Wang, Z.K. Liu, L.Q. Chen, Y.H. Chu, F. Zavaliche, R. Ramesh, Effect of substrate-induced strains on the spontaneous polarization of epitaxial  $\text{BiFeO}_3$  thin films. *J. Appl. Phys.* **101**, 114105 (2007)
51. Y.L. Li, L.Q. Chen, G. Asayama, D.G. Schlom, M.A. Zurbuchen, S.K. Streiffer, Ferroelectric domain structures in  $\text{SrBi}_2\text{Nb}_2\text{O}_9$  epitaxial thin films: electron microscopy and phase-field simulations. *J. Appl. Phys.* **95**, 6332–6340 (2004)
52. Y.L. Li, S.Y. Hu, D. Tenne, A. Soukiassian, D.G. Schlom, L.Q. Chen, X.X. Xi, K.J. Choi, C.B. Eom, A. Saxena, T. Lookman, Q.X. Jia, Interfacial coherency and ferroelectricity of  $\text{BaTiO}_3/\text{SrTiO}_3$  superlattice films. *Appl. Phys. Lett.* **91**, 252904 (2007)
53. Y.L. Li, S.Y. Hu, D. Tenne, A. Soukiassian, D.G. Schlom, X.X. Xi, K.J. Choi, C.B. Eom, A. Saxena, T. Lookman, Q.X. Jia, L.Q. Chen, Prediction of ferroelectricity in  $\text{BaTiO}_3/\text{SrTiO}_3$  superlattices with domains. *Appl. Phys. Lett.* **91**, 112914 (2007)
54. L. Hong, Y.L. Li, P.P. Wu, L.Q. Chen, Minimum tetragonality in  $\text{PbTiO}_3/\text{BaTiO}_3$  ferroelectric superlattices. *J. Appl. Phys.* **114**, 144103 (2013)
55. L. Hong, P. Wu, Y. Li, V. Gopalan, C.-B. Eom, D.G. Schlom, L.-Q. Chen, Piezoelectric enhancement of  $(\text{PbTiO}_3)_m/(\text{BaTiO}_3)_n$  ferroelectric superlattices through domain engineering. *Phys. Rev. B* **90**, 174111 (2014)
56. S.Y. Hu, L.Q. Chen, A phase-field model for evolving microstructures with strong elastic inhomogeneity. *Acta Mater.* **49**, 1879–1890 (2001)
57. S.Y. Hu, Y.L. Li, L.Q. Chen, Effect of interfacial dislocations on ferroelectric phase stability and domain morphology in a thin film: a phase-field model. *J. Appl. Phys.* **94**, 2542–2547 (2003)
58. J.D. Clayton, J. Knap, A phase field model of deformation twinning: nonlinear theory and numerical simulations. *Physica D* **240**, 841–858 (2011)
59. W. Hong, X. Wang, A phase-field model for systems with coupled large deformation and mass transport. *J. Mech. Phys. Solids* **61**, 1281–1294 (2013)
60. L. Chen, F. Fan, L. Hong, J. Chen, Y.Z. Ji, S.L. Zhang, T. Zhu, L.Q. Chen, A phase-field model coupled with large elasto-plastic deformation: application to lithiated silicon electrodes. *J. Electrochem. Soc.* **161**, F3164–F3172 (2014)